

Dedicated to the
nation, teachers,
family and friends

CERTIFICATE

It is certified that the work contained in the thesis titled "*PHASE TRANSITIONS, LOCAL STRUCTURE AND ANOMALOUS HALL EFFECT IN Ni-Mn-BASED MAGNETIC SHAPE MEMORY ALLOYS AND RELATED SYSTEMS*" by "*ANUPAM KUMAR SINGH*" has been carried out under my supervision and that this work has not been submitted elsewhere for a degree.

It is further certified that the student has fulfilled all the requirements of Comprehensive, Candidacy and SOTA for the award of the Ph.D. degree.

Date: 10-03-2022

Place: Varanasi



Dr. Sanjay Singh
(Supervisor)

**School of Materials Science & Technology
Indian Institute of Technology
(Banaras Hindu University)
Varanasi**


**Assistant Professor/सहायक-आचार्य
School of Materials Sc.& Tech./पदार्थ विज्ञान एवं प्रौद्योगिकी स्कूल
Indian Institute of Technology/भारतीय प्रौद्योगिकी संस्थान
(Banaras Hindu University), Varanasi/(क.हि.वि.), वाराणसी**

DECLARATION BY THE CANDIDATE

I, **ANUPAM KUMAR SINGH**, certify that the work embodied in this Ph.D. thesis is my own bonafide work carried out by me under the supervision of **Dr. SANJAY SINGH** for a period from **JULY 2016** to **FEBRUARY 2022** at the **SCHOOL OF MATERIALS SCIENCE AND TECHNOLOGY**, Indian Institute of Technology (Banaras Hindu University), Varanasi, India. The matter embodied in this Ph.D. thesis has not been submitted for the award of any other degree/diploma. I declare that I have faithfully acknowledged and given credits to the research workers wherever their works have been cited in my work in this thesis. I further declare that I have not wilfully copied any other's work, paragraphs, text, data, results, *etc.*, reported in journals, books, magazines, reports dissertations, thesis, *etc.*, or available at websites and have not included them in this thesis and have not cited as my own work.


Date: 10-03-2022

Place: Varanasi


(ANUPAM KUMAR SINGH)

CERTIFICATE BY THE SUPERVISOR

This is to certify that the above statement made by the candidate is correct to the best of my knowledge.


Dr. Sanjay Singh
(Supervisor)

School of Materials Science & Technology
Indian Institute of Technology
(Banaras Hindu University)
Varanasi

Assistant Professor/सहायक-आचार्य
School of Materials Sc. & Tech./पदार्थ विज्ञान एवं प्रौद्योगिकी स्कूल
Indian Institute of Technology/भारतीय प्रौद्योगिकी संस्थान
(Banaras Hindu University), Varanasi/(क.हि.वि.), वाराणसी


Dr. Chandana Rath
(Coordinator)

School of Materials Science & Technology
Indian Institute of Technology
(Banaras Hindu University)
Varanasi

Coordinator/समन्वयक
School of Materials Science & Technology/पदार्थ विज्ञान एवं प्रौद्योगिकी स्कूल
Indian Institute of Technology/भारतीय प्रौद्योगिकी संस्थान
(Banaras Hindu University), Varanasi/काशी हिन्दू विश्वविद्यालय, वाराणसी

COPYRIGHT TRANSFER CERTIFICATE

Title of the Thesis: *"Phase Transitions, Local Structure and Anomalous Hall Effect in Ni-Mn-based Magnetic Shape Memory Alloys and Related Systems"*


Candidate's Name: Mr. Anupam Kumar Singh

Copyright Transfer

The undersigned hereby assigns to the Indian Institute of Technology (Banaras Hindu University), Varanasi all rights under copyright that may exist in and for the above thesis submitted for the award of the *Doctor of Philosophy*.

Date: 10-03-2022

Place: Varanasi


(Anupam Kumar Singh)

Note: However, the author may reproduce or authorize others to reproduce materials extracted verbatim from the thesis or derivative of the thesis for author's personal use provided that the source and the Institute's copyright notice is indicated.

Acknowledgements

First and foremost, I would like to express my sincere gratitude to my esteemed supervisor, Dr. Sanjay Singh, for his super guidance, support, encouragement, and valuable suggestions throughout my Ph.D. work. His constant monitoring and interest in my work always remain a happy memory through all these years. His patience and enthusiastic approach for my training in the field of phase transitions, local structure, magnetism, and anomalous transport properties cannot be expressed in words, and I will always be thankful to him.

I would like to express my deep gratitude towards Prof. Dhananjai Pandey (SMST, IIT(BHU)) for his constant guidance, advising through many scientific discussions, and keeping me optimistic and curious throughout the research activities. I am thankful to him for sharing his experiences and ideas in this field, without which this work was not possible.

I would like to express my gratitude towards the School of Materials Science and Technology faculty members, Prof. R. Prakash, Prof. P. Maiti, Dr. C. Rath (Coordinator), Dr. A. K. Singh, Dr. C. Upadhyay, Dr. B.N. Pal, Dr. A. K. Mishra, Dr. S. K. Mishra, Dr. Nikhil Kumar, Dr. S. R. Singh, Prof. J. Kumar, and Dr. Ashish Singh for providing constant encouragement and valuable suggestions during my Ph.D. work which greatly helped me to complete my work with confidence.

I am also very thankful to my external RPEC member Dr. Saurabh Tripathi (Department of Physics, IIT (BHU)), for his valuable suggestions and help during my Ph.D. work.

I am thankful to the Department of Science and Technology (DST), Government of India, for providing the financial support to carry out synchrotron x-ray diffraction measurements at P02.1 beamline, PETRA-III, DESY, Hamburg, Germany.

I am very grateful to beamline scientist Dr. Bobby Joseph (XPRESS beamline, ELETTRA) for his kindness in providing the synchrotron x-ray diffraction data under pressure and magnetic field. I want to thank him for the important discussions, which enhanced my understanding in this field.

I wish to express my gratitude towards thank Dr. Sunil Nair (IISER Pune) and thankful to Dr. Avirup De (IISER Pune) for the fruitful collaboration in carrying out the Nernst measurements. I had great experiences working and sharing knowledge with them.

I especially want to thank Dr. Biswanath Dutta (Delft University of Technology, Netherlands) for their theoretical calculations and useful discussions.

I would like to thank Dr. Rajeev Rawat (UGC-DAE, CSR, Indore) for providing the opportunity to prepare the samples and for valuable discussions.

I wish to thank Dr. Parul Devi (Dresden High Magnetic Field Laboratory, Dresden, Germany) for the essential discussions on the biskymions.

I would also like to thank Prof. S. Arumugam and Mr. G. Lingannan (CHPR, Bharathidasan University Tiruchirappalli, India) for providing the transport data under pressure and for useful discussions.

I want to thank Dr. Satadeep Bhattacharjee and Dr. Seung-Cheol Lee (IKST, Bangalore, India) for the fruitful discussions.

I am also very grateful to beamline scientists Dr. M. Etter and Dr. J. Tseng for their kind help in setting the experiments for synchrotron x-ray diffraction measurements at PETRA-III, DESY.

I want to thank G. Bais and M. Polentarutti of ELETTRA-Sincrotrone Trieste for their help in the setup of synchrotron x-ray diffraction measurements under the magnetic field.

I would like to thank the Central Instrument Facility, IIT (BHU), for the different characterizations of the samples.

I wish to express my extreme gratefulness towards my seniors: Dr. Keshav Kumar, Mrs. Pragya Singh, Dr. Arun Kumar and Gaurav Chandra Pandey, for helping me during the whole period of my Ph.D. work, whenever I needed. I am also thankful to my seniors, Dr. Anar Singh, Dr. Pappu Kumar, and Dr. Shushil Kumar, for their constant support and motivation.

I want thanks to all my friends: Sudheer, Sameer, Abhay, Avinash, Rajnish, Gaurav, Archita, Mohit, Aravintha, Amit, Bishnu, Shyam, Jay Prakash, Pragati, Jais, Manish, Ajay, Kanchan, Pragyananad, Deepti, Andeep, Om Prakash, Ravi Prakash, Nikhil, Ravi Ojha, Aniruddh, Ajay, Abhishek, and Ankit for giving me moral support, pleasant company and confidence to complete my work with a 'smile.'

I especially thank my juniors: Krishna Kant Dubey, Nisha Shahi, Gaurav K. Shukla, and Vishal Saini, for their constant support, help, and motivation throughout my Ph.D. I am also thankful to all other juniors: Shivani, Pankaj, Nidhi, Payal, Vikas, Gaurav, Ishita, Aditya, for providing a pleasant, encouraging, and friendly environment.

I am also very thankful to the technical and non-technical staff of my school: Mr. Amarnath, Dharmendra, Kallu Ram, Ashwani, Sitaram Tiwari, Samir Dubey, Amod Kumar Pandey, Mahendra, Dharmendra, Waris, Awanish, Ankit, Sudhakar, Dinesh, Sajan and Jaislaal for the cooperation and help. Special thanks to Mr. Sameer Dubey for the help throughout my Ph.D. work.

*I would like to express my heart-felt gratitude towards my parents and family members for their constant encouragement, moral support, and blessing at every step of my life, which cannot be expressed in words. My special thanks to my beloved wife, Mrs. Damini Singh, for her affection and mental support to me throughout my Ph.D. journey. My love and wishes are always with her. Finally, I thank **GOD** for giving me the strength to complete my thesis successfully.*

Date: 10-03-2022

(Anupam Kumar Singh)

Place: Varanasi

Table of Contents

Acknowledgements	i
Table of Contents	v
List of Figures.....	ix
List of Tables	xxiii
List of Abbreviations	xxv
List of Symbols	xxix
Preface.....	xxxiii
1 Chapter 1: Introduction and Literature Review	1
1.1 Martensite Phase Transition	1
1.2 Shape Memory Alloys.....	5
1.3 Magnetic Shape Memory Alloys.....	7
1.4 Ni-Mn-based Magnetic Shape Memory Alloys	10
1.4.1 Phase Transitions in Ni-Mn-Ga Magnetic Shape Memory Alloys.....	10
1.4.2 Phase Transitions in Ni-Mn-In Magnetic Shape Memory Alloys	15
1.4.3 Premartensite (Precursor) Phase in Ni-Mn-based Magnetic Shape Memory Alloys..	16
.....	16
1.5 Anomalous and Topological Hall Effect.....	20
1.6 Magnetic Shape Memory Alloys with Hexagonal Austenite Phase	26
1.7 Objective of the Present Work	30
2 Chapter 2: Synthesis and Experimental Methods	33
2.1 Synthesis Procedure	33
2.2 X-ray Diffraction.....	36
2.3 Scanning Electron Microscope and Energy Dispersive Analysis of X-rays.....	37
2.4 Differential Scanning Calorimetry	40
2.5 Magnetic Measurements	41
2.6 Magnetoresistance and Hall Measurements.....	45
2.7 Synchrotron X-ray Powder Diffraction.....	50
2.7.1 Linac	51
2.7.2 Booster Ring	51

2.7.3	Storage Ring.....	51
2.7.4	Beamlines.....	51
2.7.5	P02.1 Beamline of PETRA-III.....	52
2.7.6	Xpress Beamline of ELETTRA.....	54
3	Chapter 3: A Pair Distribution Function Study of Ni₂MnGa Magnetic Shape Memory Alloy: Evidence for the Precursor State of the Premartensite Phase	57
3.1	Introduction	57
3.2	Experimental Section	61
3.3	Atomic Pair Distribution Function Method	62
3.4	Results and Discussion.....	65
3.4.1	Magnetization	65
3.4.2	Arrott Plot, Critical Isotherm and Universal Curve	68
3.4.3	Temperature Dependent High-Resolution Synchrotron X-ray Powder Diffraction.....	75
3.4.4	Temperature dependent atomic pair distribution function analysis.....	79
3.5	Conclusions	91
4	Chapter 4: Intrinsic Anomalous Hall Conductivity and Topological Hall Effect in Ni₂MnGa Magnetic Shape Memory Alloy.....	93
4.1	Introduction	93
4.2	Experimental Section	97
4.3	Results and Discussion.....	99
4.3.1	Phase purity.....	99
4.3.2	Temperature and Magnetic Field Dependent Magnetization.....	100
4.3.3	Resistivity and Magnetoresistance.....	104
4.3.4	Anomalous Hall Effect	106
4.3.5	Topological Hall Effect.....	112
4.4	Conclusions	119
5	Chapter 5: Stabilization of the Premartensite Phase in Ni₅₀Mn₃₄In_{16-x}Al_x (x = 0.5, 0.8) Magnetic Shape Memory Alloys.....	121
5.1	Introduction	121
5.2	Experimental Section	125
5.3	Results and Discussion.....	127
5.3.1	Phase Purity and Phase Transition.....	127

5.3.2	Magnetization and High-Resolution Synchrotron X-ray Powder Diffraction	130
5.4	Conclusions	143
6	Chapter 6: Temperature and Pressure-Induced Phase Transition and Magnetoelastic Coupling in the Hexagonal NiMnGa.....	145
6.1	Introduction	145
6.2	Experimental Section	151
6.3	Results and Discussion.....	152
6.3.1	Phase Purity	152
6.3.2	Ferromagnetic to Paramagnetic Phase Transition Behavior	153
6.3.3	Spin Reorientation Transition Behavior	160
6.3.4	Temperature Dependent Structure Investigation	163
6.3.5	Magnetoelastic Coupling	169
6.3.6	Bond Length and Bond Angle	172
6.3.7	Thermal Expansion Behavior	176
6.3.8	Structural Investigation Under Hydrostatic Pressure.....	179
6.4	Conclusions	187
7	Chapter 7: Signature of Skyrmions and Evidence for the Local Noncentrosymmetric Crystal Structure in Hexagonal NiMnGa.....	189
7.1	Introduction	189
7.2	Experimental Section	193
7.3	Results and Discussion.....	193
7.3.1	Temperature Dependent AC-Susceptibility	193
7.3.2	Signature of the Skyrmions with Hysteretic Nature using Magnetic Field Dependent AC-Susceptibility Measurements.....	195
7.3.3	Temperature Dependent High- <i>Q</i> Synchrotron X-ray Powder Diffraction	199
7.3.4	Temperature Dependent Atomic Pair Distribution Function Analysis.....	201
7.4	Conclusions	215
8	Chapter 8: Summary and Suggestions for Future Work	217
8.1	Summary	217
8.2	Suggestions for Future Work	219
	References	223
	List of Publications	263

List of Figures

Figure 1.1: Schematic diagram of FCC austenite to BCT martensite transformation via Bain distortion. The xyz and XYZ represent the axes of the parent FCC austenite and BCT martensite phase, respectively. The lattice parameter (LP) of FCC lattice is labelled by a_0 , while LP of BCT lattice are a and c [16]..... 2

Figure 1.2: Lattice deformation from austenite to the martensite phase accompanying shear. (a) No lattice invariant shear, (b) Slip shear, and (c) Twinning shear[14]. (d) A more simplified model of austenite to the martensite phase transformation[16]. 3

Figure 1.3: (a) Austenite to martensite phase transition with temperature change. The M_s , M_f , A_s , and A_f indicate the martensite start, martensite finish, austenite start, austenite finish temperatures, respectively. The H represents the width of the thermal hysteresis. (b) Schematic diagram of Gibbs free energy (G) relationship during the martensite transformation[19]. ΔT_s is the supercooling driving temperature for the forward martensite transformation. The subscripts P and M stand for the parent austenite and martensite phases, respectively, while T_0 indicates the equilibrium temperature. 4

Figure 1.4: Schematic diagram of shape memory effect and superelastic behavior during cooling, heating, loading, and unloading are depicted. The states (i), (ii), and (iii) represent the austenite, twinned martensite, and detwinned martensite phases. Labels A_f and M_f indicate the austenite finish and martensite finish temperatures, respectively. The black curve represents a wire whose shape changes in (i) and (iii)..... 7

Figure 1.5: Schematic diagram of magnetic shape memory effect with application of magnetic field (H). The states (i), (ii), and (iii) represent the twinned martensite with no magnetic field, twinned martensite with field H , and detwinned martensite with field H , respectively. The MCA stands for magnetocrystalline anisotropy..... 8

Figure 1.6: Schematic diagram of unit cells of austenite phase (A) for Ni_2MnGa MSMA. The inset (i), (ii), and (iii) depicts the unit cells of body centered tetragonal martensite, $3M$ modulated premartensite (PM), and $7M$ modulated martensite (M) phases, respectively. 12

Figure 1.7: Phase diagram of Ni-Mn-Ga MSMA for (a) deficient Ni and excess Mn, (b) excess Ni and deficient Mn and (c) excess Mn and deficient Ga composition. The FM and PM stand for

ferromagnetic and paramagnetic, while T_C , T_M , and T_{PM} indicate the *PM* to *FM*, martensite, and premartensite phase transition temperature, respectively[93]. 14

Figure 1.8: Phase diagram of Ni-Mn-In MSMA. The FM and PM stands for ferromagnetic and paramagnetic while T_C^A , T_C^M and M_s indicate the Curie temperature of the austenite, Curie temperature of the martensite, and martensite start temperature, respectively. Label $L1_0$ represents the $L1_0$ -type tetragonal structure[98]. 16

Figure 1.9: (a) Schematic illustration of Hall effect, where I, H, and V stands for current, magnetic field, and Hall voltage, respectively[152] and (b) Hall resistivity (ρ_{xy}) with magnetic field for a nonmagnetic conductor[153]. 21

Figure 1.10: (a) Schematic illustration of anomalous Hall effect (AHE)[152] and (b) Hall resistivity (ρ_{xy}) with magnetic field for a ferromagnetic conductor, where $R_S M$ is the zero-field intercept and is related to the AHE (see eq. (1.1) for more detail)[153]. 22

Figure 1.11: Schematic illustrations of intrinsic, side jump, and skew scattering mechanism to anomalous Hall effect[159]. 23

Figure 1.12: The schematic diagram of topological hall effect (THE). (a) Turning of electron trajectory on passing through a magnetic texture like skyrmion. The electron's spin orientation follows the spin orientation of the skyrmion texture. (b) Topological hall resistivity vs magnetic field plot, where arrow indicated the direction of field sweeping. Insets in (b) show positive and negative magnetic fields skyrmions with reversed spin texture [184]. 25

Figure 2.1: (a) Real image of sample preparation unit at the School of Materials Technology, IIT (BHU), Varanasi, India. (b) An enlarged view of the vacuum arc melting furnace. 35

Figure 2.2: Schematic diagram of x-ray diffraction by a set of lattice planes of the crystal. 36

Figure 2.3: (a) A real image of temperature dependent x-ray diffractometer in the School of Materials Science and Technology, IIT (BHU). (b) An enlarged view of the machine part. 37

Figure 2.4: A schematic diagram of working principle of scanning electron microscope[236]... 39

Figure 2.5: A schematic mechanism of characteristic x-rays emission from inner shells of an atom by primary electron beam[237]. 39

Figure 2.6: A schematic diagram of the working principle of DSC[238]. 41

Figure 2.7: A schematic diagram of the operating principle for the VSM option of PPMS[239].42

Figure 2.8: A schematic diagram of ACMS II coil set[240], where different coils are indicated.44

Figure 2.9: The schematic diagram of magnetic flux detection by SQUID, where $\Delta\phi$ is the change in flux and ϕ_0 is flux quanta[241]..... 45

Figure 2.10: A typical schematic diagram of (a) Longitudinal voltage and (b) Hall (transverse) voltage measurement setup, where I_+ , I_- , V_+ , and V_- , indicate positive current, negative current, positive potential, and negative potential contacts respectively while H , V_L , and V_H represent the magnetic field, longitudinal voltage, and Hall voltage, respectively..... 46

Figure 2.11: A real image of a sample mounted for magnetotransport measurements using the four-probe method in ETO of PPMS at School of Materials Science and Technology, IIT (BHU). ... 47

Figure 2.12: The real image of CFMS setup at School of Materials Science and Technology, IIT (BHU). 49

Figure 2.13: The real image of sample holder for magnetoresistance measurement using CFMS at School of Materials Science and Technology, IIT (BHU). 49

Figure 2.14: A schematic diagram of synchrotron light source and beamlines[245]. 52

Figure 2.15: (a) Schematic diagram of optics of P02.1 beamline of PETRA-III, DESY[246]. (b) Real image of mounted capillary during measurement at P02.1 beamline of PETRA-III, DESY. 53

Figure 2.16: (a) Schematic diagram of diamond anvil cell (DAC). The (b) and (c) show the real image of the experimental hutch and ruby fluorescence setup at the Xpress beamline of ELETTRA. The inset above (c) depicts the automation of the pressure membrane system. 55

Figure 3.1: Temperature dependence of the direct dc magnetization of Ni_2MnGa , measured at 100 Oe in the zero-field cooled warming (ZFCW) cycle at the rate of (a) 4 K/min and (c) 1 K/min and (b) temperature dependence of the real part of the ac-susceptibility of Ni_2MnGa measured at 333 Hz in the ZFCW (black color), field cooled (FC; red color), and field cooled warming (FCW; blue color) cycles. The inset of (a) gives an enlarged view for $235 \text{ K} \leq T \leq 365 \text{ K}$ range to clearly show the dip in magnetization at the premartensite phase transition temperature $T_{PM} \sim 260 \text{ K}$ as well as the anomalously decreasing behavior of magnetization below the ferromagnetic (FM) Curie temperature (T_C). The insets (i) and (ii) of (b) show an enlarged view around the premartensite and FM transition temperatures, respectively. The inset of (c) shows the thermal hysteresis across FM T_C using two independent measurements labeled as I and II..... 66

Figure 3.2: (a) The isothermal (magnetic field dependent) magnetization data around Curie temperature ($T_C \sim 371 \text{ K}$). (b) The Arrott plots, obtained from (a). The inset of (b) shows the

enlarged view around the lower field region, revealing the negative slope guided by a dotted blue arrow. 69

Figure 3.3: The behavior of $\ln(M)$ with $\ln(H)$ around $T_C \sim 371$ K. The red line represents the linear fitting at the higher field at 370 K. The significant deviation from the linearity at the lower magnetic field regions is indicated by extrapolated wine color line..... 70

Figure 3.4: Isothermal entropy change versus temperature across the magnetic phase transition. The vertical dotted blue line marks the peak value, which appears at $T_C \sim 371$ K. 71

Figure 3.5: (a) The variation of the peak value of entropy change (ΔS_{pk}) (obtained from Figure 3.4) with change in the magnetic field. (b) The red line indicates the fit using power law ($\Delta S_{pk} = k H^n$). The variation of ΔS_{pk} with the rescaled magnetic field (H^n). The blue line represents the deviation from linearity at the lower field region. 72

Figure 3.6: The normalized entropy change ($\Delta S_{iso}/\Delta S_{pk}$) versus rescaled temperature (θ) 74

Figure 3.7: (a) High-resolution SXRPD patterns at various temperatures in the temperature range 260 K to 400 K. The inset (i) shows the enlarged view around the most intense Bragg peak of the cubic austenite phase at various temperatures while the inset (ii) depicts a highly magnified view around the most intense peak at 260 K showing the appearance of satellite peaks corresponding to the premartensite phase, which are marked as “PM”. The panels (b) and (c) show the observed (black circles), calculated (continuous red line), and difference profiles (continuous green line at the bottom) obtained after Rietveld refinement using SXRPD data at 400 K and 270 K, respectively, while the blue tick bars indicate the Bragg peak positions and R_{wp} is the weighted agreement factor. The inset in (b) and (c) show the quality of Rietveld fit around the most intense peak. 76

Figure 3.8: The variation of the (a) unit cell volume (V) with temperature showing volume contraction at $T \leq T_C$, (b) linear volume expansion coefficient (α_V), obtained using the V versus T plot, (c) cubic volume strain ($\Delta V/V$) with M_s^2 in the temperature range of $260 \text{ K} < T < 370 \text{ K}$, and (d) spontaneous magnetization M_s , measured at 7 Tesla field, as a function of temperature. The dotted line (blue) in (a) is the extrapolated region of the linear expansion behavior above T_C , while the dotted line in (c) corresponds to the least-squares linear fit. 78

Figure 3.9: (a) The observed (black circles), calculated (continuous red line) and difference profiles (green line), Bragg peak positions (blue ticks), and weighted agreement factor (R_{wp}) obtained after

Rietveld refinement of the cubic austenite phase in the $Fm\bar{3}m$ space group using high- Q SXRPD data at 400 K. (b) The reduced structure function $F(Q)$ versus Q 80

Figure 3.10: The experimental (dark black dots connect with black line) and calculated (continuous red line) PDFs and their difference (blue line at the bottom) obtained by real space structure refinement using cubic space group $Fm\bar{3}m$ in the (a) SR and (b) LR regimes at 400K, and (c) SR and (d) LR regimes at 300 K. The insets in (a) and (c) show an enlarged view of the PDF fits around 5.4 Å. The asterisk (*) marked peak is a ripple due to the truncation of the Fourier series. 81

Figure 3.11: Experimental PDFs in the SR regime at various temperatures from 400 K to 260 K. The atomic pairs contributing to the individual peaks are indicated below the blue arrow line. The asterisk (*) marked peak is a ripple due to the truncation of the Fourier series. The inset shows an enlarged view around 5.4 Å, where the black arrow is to guide to the emergence of new pair of interatomic distance while the blue arrow shows the shift of the minima towards the higher r side. 84

Figure 3.12: The experimental (dark black dots connected with black line) and calculated (continuous red line) PDFs and their difference (blue line at the bottom) obtained by real space structure refinement at 260 K using $3M$ modulated orthorhombic premartensite phase space group $Pnmn$ in the (a) SR and (b) SR+LR regimes. The PDF fits at 300 K using the same space group ($Pnmn$) in the (c) SR and (d) the SR+LR regimes. The insets in (a), (b), (c), and (d) show an enlarged view of the PDF fit around 5.4 Å. The asterisk (*) marked peak is a ripple due to the truncation of the Fourier series. 86

Figure 3.13: The experimental (dark black dots connected with black line) and calculated (continuous red line) PDFs and their difference (blue line at the bottom) using the $3M$ modulated orthorhombic premartensite phase space group ($Pnmn$) in the temperature range 330 to 270 K obtained by real space structure refinement. The left panel ((a) to (g)) shows fits up to the correlation length (ζ) for which the premartensite phase structure is able to account for the peak around 5.4 Å, as shown in the insets. The right panel ((h) to (n)) depicts the fits to a distance, which is greater than the correlation lengths. The misfit for the peak around 5.4 Å is quite evident from the insets of (h) to (n). 90

Figure 3.14: The correlation length (ζ) of the premartensite phase as a function of temperature. The black dotted line shows the slowly increasing trend of ζ in the temperature range 330 to 270

K. The sharp increase in ξ at $T_{PM} \sim 260$ K is shown by the dotted blue line. Below 260 K, ξ tends towards its saturation value for the long-range ordered premartensite phase..... 91

Figure 4.1: The observed (dark black dots), calculated (continuous red line), and difference profiles (green bottom line) obtained after Rietveld refinement of cubic austenite phase in the $Fm\bar{3}m$ space group using x-ray powder diffraction data at room temperature of Ni_2MnGa . Above the difference profile, the vertical tick marks represent the Bragg peak positions whose miller indices are indicated. The inset (i) depicts an enlarged view of the fit at the low 2θ -range. The inset (ii) shows a BSE image of Ni_2MnGa 100

Figure 4.2: (a) Temperature dependence of dc magnetization (M) of Ni_2MnGa , measured at 100 Oe in the zero-field cooled warming (ZFCW; black color), field cooled (FC; red color), and field cooled warming (FCW; blue color) cycles. The inset in (a) depicts an enlarged view around paramagnetic to ferromagnetic transition. The T_M , T_{PM} , T_{onset} and T_C (indicated in the inset) represent the martensite, premartensite, onset of ferromagnetic, and ferromagnetic transition temperatures, respectively. The arrows are to guide the cooling and warming cycles. (b) The magnetic field dependence of magnetization of Ni_2MnGa , measured at the indicated temperatures (385-2 K), wherein inset depicts the temperature dependency of the saturation magnetization (M_S). 103

Figure 4.3: (a) Temperature dependence of longitudinal resistivity (ρ_{xx}) of Ni_2MnGa , measured in cooling and warming cycles at 0 and 1 T. The insets depict an enlarged view around the martensite phase transition where cooling and warming cycles are indicated by arrows. The T_{PM} indicates the premartensite transition temperature. (b) The magnetic field dependence of magnetoresistance (MR) of Ni_2MnGa , measured at the indicated temperatures (385-2 K). 105

Figure 4.4: (a) The magnetic field dependence of resistivity corresponding to the anomalous Hall effect (ρ_{AHE}) of Ni_2MnGa , measured at the indicated temperatures (385-2 K). (b) Variation of anomalous Hall resistivity divided by saturation magnetization (ρ_{AH}/M_S) with longitudinal resistivity (ρ_{xx}) and (c) their logarithm value (dark black dots) in the martensite and in both austenite and premartensite (“A+PM”) phases. The blue line represents in (b) fitting using equation $\rho_{AH}/M_S = a\rho_{xx} + b\rho_{xx}^2$ and (c) linear fit wherein the value of slope (β) of the linear fit is indicated. (d) Temperature dependency of the anomalous Hall conductivity (σ_{AH}). (f) Temperature dependency of scaling coefficient ($S_H = \sigma_{AH}/M_S$), where red and blue line represent the temperature

independency of S_H in the martensite and “A+PM” phases, respectively. The austenite, premartensite (PM), and martensite phases are separated by dashed lines in (d) and (f). 108

Figure 4.5: The magnetic field dependence of (a)-(i) experimental (ρ_{xy}^{exp} ; dark black dots connected with line) and calculated Hall resistivity (ρ_{xy}^{cal} ; red continuous line) and (j) topological Hall resistivity (ρ_{xy}^T) of Ni_2MnGa at the indicated temperatures. The (k) depicts the contour mapping of the magnitude of ρ_{xy}^T as a function of the magnetic field (H) and temperature (T). 113

Figure 4.6: Temperature dependence of (a) maximum value magnitude of topological Hall resistivity (ρ_{xy}^{max}) and (b) anisotropy constant (K_u) of Ni_2MnGa . The austenite, premartensite (PM), and martensite phase regions are separated by vertical dashed lines. Green, red and blue color dotted lines are to guide the behavior of ρ_{xy}^{max} and K_u in the austenite, PM and martensite phases, respectively. 117

Figure 5.1: The observed (dark black dots), calculated (continuous red line), and difference profiles (continuous green line) obtained after Le Bail refinement using laboratory source XRD data at 300 K for (a) the martensite phase in the $P2/m$ space group for $Ni_{50}Mn_{34}In_{15.5}Al_{0.5}$ and (b) for the cubic austenite phase in the $Fm\bar{3}m$ space group for $Ni_{50}Mn_{34}In_{15.2}Al_{0.8}$. Above the difference profile, the vertical tick marks represent the Bragg peak positions in (a) and (b). The inset of (a) depicts an enlarged view of fit around the most intense Bragg peak, while the inset of (b) shows an enlarged view of fit around the (111) and (200) Bragg reflections. The BSE image for (c) $Ni_{50}Mn_{34}In_{15.5}Al_{0.5}$ and (d) $Ni_{50}Mn_{34}In_{15.2}Al_{0.8}$ 129

Figure 5.2: The DSC data for (a) $Ni_{50}Mn_{34}In_{15.5}Al_{0.5}$ and (b) $Ni_{50}Mn_{34}In_{15.2}Al_{0.8}$. The arrows in (b) and (c) indicate the heating and cooling cycle. The magnetic field dependent magnetization ($M(H)$ loop) for (c) $Ni_{50}Mn_{34}In_{15.5}Al_{0.5}$ at 5 K and (d) $Ni_{50}Mn_{34}In_{15.2}Al_{0.8}$ at 2 K. The value of saturation magnetic moment (M_S) is indicated in (c) and (d). 130

Figure 5.3: (a) The temperature dependent dc-magnetization at 500 Oe for Al free $Ni_{50}Mn_{35}In_{15}$ (taken from reference[91]). The temperature dependent real part of ac-susceptibility for (b) $Ni_{50}Mn_{34}In_{15.5}Al_{0.5}$ and (c) $Ni_{50}Mn_{34}In_{15.2}Al_{0.8}$ MSMA. The insets are enlarged view around 300 K for the field cooled protocol. The T_M , T_{PM} , T_C^M and T_C represent the martensite transition temperature, premartensite transition temperature, Curie temperature of the martensite phase, and Curie temperature of the austenite phase, respectively. The ZFCW, FC, and FCW correspond to

measurements performed during warming on the zero-field cooled sample, during field cooling, and during warming on the field cooled sample, respectively..... 132

Figure 5.4: Typical SXRPD patterns of $\text{Ni}_{50}\text{Mn}_{34}\text{In}_{15.5}\text{Al}_{0.5}$ MSMA in the (a) austenite, (b) premartensite, and (c) martensite phases. An enlarged view around the most intense (220) Bragg peak for the austenite and the premartensite (PM) phases, given in inset (i) of (a) and (b), respectively, reveal the appearance of the satellite peaks (indicated by ‘PM’ in the inset (i) of (b)) due to 3M like modulation in the PM phase. Untruncated view of the (220) cubic peak for the austenite and PM phases, given in inset (ii) of (a) and (b), respectively, reveal the absence of Bain distortion in the PM phase. The inset of (c) depicts the splitting of the most intense (220) cubic peak and appearance of the satellite peaks due to Bain distortion and 3M like modulation of the martensite (M) phase. The observed (dark black dots), calculated (continuous red line), and difference patterns (continuous green line), obtained after Le Bail refinement using the SXRPD data for the (d) cubic austenite, (e) 3M modulated PM, and (f) 3M modulated martensite phases in the $Fm\bar{3}m$, $P2/m$, and $P2/m$ space groups, respectively, for $\text{Ni}_{50}\text{Mn}_{34}\text{In}_{15.5}\text{Al}_{0.5}$. The vertical ticks above the difference profile represent the Bragg peak positions. The insets (i) and (ii) of (a) show an enlarged view of fit around the (111) and (200) Bragg reflections and around the most intense Bragg peak, respectively. The inset of (e) and (f) shows fits around the most intense Bragg peak region in a magnified scale. The satellite peaks of the PM phase are marked as ‘PM’ at 310 K in the inset of (b) and (e). The peaks related to the martensite phase are marked as ‘M’ at 110 K in the inset of (c) and (f)..... 133

Figure 5.5: (a) The laboratory source ($\text{CuK}\alpha$) XRD data at indicated temperature (300 to 13 K) for $\text{Ni}_{50}\text{Mn}_{34}\text{In}_{15.5}\text{Al}_{0.5}$ MSMA. (b) An enlarged view around the most intense Bragg peak region of (a). The peaks related to the martensite phase are marked as ‘M’ in (b)..... 135

Figure 5.6: The SXRPD patterns of $\text{Ni}_{50}\text{Mn}_{34}\text{In}_{15.2}\text{Al}_{0.8}$ are shown in (a) at (i) 400 K, (ii) 220 K, and (iii) 100 K. The insets show an enlarged view around the most intense Bragg peak to reveal the satellite peaks of the premartensite (PM) phase. The enlarged view around the most intense cubic peak (220) at the various temperatures in the range 400-100 K are given in (b) and (c). The arrows in (c) indicate the temperature dependent shifts of the PM satellite peak positions. Note the gradual sharpening of the satellite peaks in (c) on lowering the temperature. (d) An enlarged view around the most intense (220) cubic peak at selected temperatures reveal the appearance of the most intense satellite peak of the PM phase at $T \sim 300$ K, indicated by an arrow. (e) Untruncated

SXRPD profiles of the (220) cubic Bragg peak is depicted in the 400 to 100 K range. The satellite peaks of the PM phase are marked as ‘PM’ in the inset of (ii) and (iii) of (a) and in (c). 137

Figure 5.7: The laboratory source (CuK α) XRD data of Ni₅₀Mn₃₄In_{15.2}Al_{0.8} alloy at indicated temperatures (300 to 13 K) wherein the inset shows an enlarged view around the most intense Bragg peak. 138

Figure 5.8: The observed (dark black dots), calculated (continuous red line), and difference patterns (continuous green line) obtained after Le Bail refinement using SXRPD pattern of Ni₅₀Mn₃₄In_{15.2}Al_{0.8} MSMA for the (a) cubic austenite phase at 400 K and (b) 3M modulated premartensite (PM) phase at 100 K in the $Fm\bar{3}m$ and $P2/m$ space groups, respectively. The vertical tick marks above the difference profile represent the Bragg peak positions in (a) and (b). The inset of (a) shows the presence of (111) and (200) Bragg reflections characteristic of the L2₁ ordering in the cubic austenite phase. The inset of (b) shows an enlarged view of the fit around the most intense Bragg peak and satellite reflections (marked as ‘PM’ with their indices) related to the 3M modulated PM phase. The temperature dependence of the dc magnetization, measured on zero-field cooled sample during warming cycle, is shown in (c) for different magnetic fields. The enlarged view of (c) around the FM T_C, shown in (d), reveals a skewed diffuse peak due to the PM transition. The variation of the PM transition temperature (T_{PM}) with the magnetic field is shown in (e). 140

Figure 5.9: (a) High-resolution SXRPD pattern collected at 294 K under zero magnetic field (black dots connected with a continuous line) and an external magnetic field of 2500 Oe (red squares connected with a continuous line) for Ni₅₀Mn₃₄In_{15.2}Al_{0.8}. The inset of (a) shows an enlarged view of the lower 2 θ -range (2-12.5°). (b) An enlarged view of encircled region of (a) (guided by arrow). Note the disappearance of the satellite peaks related to the premartensite (PM) phase under the magnetic field. (c) Image of magnets setup used in measurement, where (i), (ii), (iii), and (iv) indicate the magnets, capillary position, plastic for support, and clay for positioning the magnets centered with respect to the capillary, respectively (shown by arrow). The ‘*’ in the inset of (a) and ‘PM’ in (b) indicate the extra peaks related to the setup of magnets and satellite peaks related to the PM phase, respectively. 142

Figure 6.1: The observed (filled black circles), calculated (continuous red line), and difference (bottom green line) profiles obtained after Rietveld refinement using laboratory x-ray powder diffraction data at room temperature using the hexagonal structure with $P6_3/mmc$ space group. The

vertical ticks above the difference profile represent the Bragg peak positions. The “ R_{wp} ” is the weighted agreement factor of the fitting. The inset depicts a unit cell structure of NiMnGa. ... 153

Figure 6.2: The magnetization vs temperature ($M(T)$) plot for an applied field of 100 Oe under zero-field cooled warming (ZFCW) cycle. Inset (i) depicts the enlarged view of $M(T)$ in the temperature range of 150 K to 330 K where the arrow shows the decreasing behavior of $M(T)$ below ferromagnetic transition temperature (T_C), the red line shows deviation below 180 K and dotted blue lines are showing the spin reorientation transition (SRT) region with starting at ~ 210 K. Inset (ii) depicts the $M(T)$ measured at a high applied field (5 Tesla) under the ZFCW cycle. 155

Figure 6.3: (a) $M(T)$ at different magnetic applied fields under ZFCW, FC, and FCW cycles indicated by black, olive, and blue color, respectively. (b) An enlarged view of (a) around T_C at the indicated field, where ZFCW and FCW cycles are completely superimposed, while the arrow indicates the FC and FCW cycles. The ZFCW, FC, and FCW correspond to measurements performed during warming on the zero-field cooled sample, during field cooling, and during warming on the field cooled sample, respectively. 157

Figure 6.4: The enlarged view of Figure 6.3(a) around T_C only for the ZFCW cycle (indicated by arrow) at the indicated fields. The red lines indicate the extrapolation of magnetization for both above and below T_C where the intersection point of red lines is considered as the onset temperature of T_C (T_{onset}) at each field. The obtained T_{onset} at each field is shown in the inset, where the blue line represents the linear fitting. 158

Figure 6.5: (a) The isotherms ($M(H)$) around T_C in the temperature range of 378-330 K, in the 2 K temperature interval, under the cooling cycle. (b) The Arrott plots (H/M vs M^2 plots) using $M(H)$. Figs. (c) and (d) depict enlarged views of the Arrott plots at the low field region at the indicated temperatures. The arrow in (c) is to guide the negative slope. The change of sign of curvature around $T_{mid} \sim 342$ K is visible in (d). 159

Figure 6.6: The enlarged view of $M(T)$ (given in Figure 6.3(a)) at the indicated fields around spin reorientation transition (SRT) for (a) ZFCW cycle and (b) FC cycle. The (c) depicts an enlarged view of $M(T)$ around SRT for FC and FCW cycles guided by the arrow at 2000 Oe of the applied field. The (d) depicts the field dependence of start of the SRT temperature (T_{SRT}^S) (obtained from ZFCW curve). 161

Figure 6.7: (a) Isothermal $M(H)$ around T_{SRT} in the 170-230 K temperature range in the 5 K temperature interval. (b) Arrott plots using $M(H)$ around T_{SRT} . The inset in (a) and (b) depict an enlarged view at the region of the high field of $M(H)$ and at the low field region of the Arrott plots.

..... 162

Figure 6.8: (a) The observed (filled black dots), calculated (continuous red line), and difference (bottom green line) profiles obtained after Rietveld refinement using synchrotron x-ray powder diffraction (SXRPD) data at room temperature using the hexagonal structure with $P6_3/mmc$ space group. The vertical blue ticks above the difference profile represent the Bragg peak positions. The inset of (a) depicts an enlarged view of the most intense Bragg peak region. (b) The SXRPD patterns at indicated temperatures. The inset of (b) depicts the enlarged view of the most intense Bragg peak region. (c) The enlarged view of SXRPD data around intense Bragg peak region in the 110-400 K range in the temperature interval of 5 K. 164

Figure 6.9: (a) The temperature dependent (300 to 15 K) laboratory source x-ray diffraction patterns of MnNiGa. (b) An enlarged view of (a) around the most intense Bragg peak region. The miller indices of both major peaks are indicated near the bottom-most pattern in (b). 165

Figure 6.10: Temperature dependent behavior of (a) lattice parameters (a & c), (b) c/a ratio and (c) unit cell volume (V). The temperature derivative of a , c , and V are given in (d) da/dT , (e) dc/dT and (f) dV/dT , respectively. The blue curve in (d), (e), and (f) represent a smoothen behavior. The transition temperatures ($T_{SRT} \sim 200$ K and $T_C \sim 350$ K) are guided by the vertical dotted line in (a)-(f). 168

Figure 6.11: The unit cell volume (V) of hexagonal phase vs temperature plot indicated by black circles. The solid red line indicates the theoretically modeled unit cell volume (V_{cal}) using the Debye-Grüneisen equation. The grey arrow indicates the deviation between V and V_{cal} . The bulk hexagonal strain ($\Delta V/V$) vs square of spontaneous magnetization (M_S^2) plots are shown in the inset (i) for 350-300 K, inset (ii) for 300-260 K, and inset (iii) for 260-180 K, where the blue line represents the linear fitting. 172

Figure 6.12: The bond length corresponding to (a) Ni-Ga, (b) Mn-Mn, and (c) Ni-Mn or Ga-Mn pairs. The temperature derivative of (d) Ni-Ga, (e) Mn-Mn, and (f) Ni-Mn or Ga-Mn, pairs. The blue curve in (d)-(f) represents a smoothen behavior. The transition temperatures $T_C \sim 350$ K and $T_{SRT} \sim 200$ K are guided by the vertical dotted line. 174

Figure 6.13: (a) Temperature dependency of bond angle corresponding to Mn1-Ni-Mn2 and Ni-Mn1-Mn2. The slope change around $T_C \sim 350$ K and $T_{SRT} \sim 200$ K are guided by the vertical dotted line. (b) The unit cell of NiMnGa, where the position of atoms involved for bond lengths (shown in Figure 6.12) and bond angles (shown in Figure 6.13(a)) are indicated (by arrows and angle) for the sake of visualization..... 175

Figure 6.14: Thermal expansion vs temperature plot corresponding to (a) a -parameter ($\Delta a/a$), (b) c -parameter ($\Delta c/c$) and (c) unit cell volume ($\Delta V/V$). The blue curve represents smoothed behavior. The anomalous, positive, and zero thermal expansion regions are guided by dashed lines and red arrows. The ZTE, ATE, and PTE represent the zero-thermal expansion, anomalous thermal expansion, and positive thermal expansion, respectively. The thermal expansion coefficient corresponding to a -parameter, c -parameter, and unit cell volume is indicated by α_a , α_c and α_V , respectively. 178

Figure 6.15: The observed (black spheres), calculated (continuous red line), and difference profiles (bottom green line) obtained after Rietveld refinement using synchrotron x-ray powder diffraction pattern at the ambient condition in the $P6_3/mmc$ space group of NiMnGa. The vertical tick marks above the difference profile represent the Bragg peak positions. The “ R_{wp} ” represents the weighted agreement factor of the fitting. The miller indices are given above each reflection. 180

Figure 6.16: (a) The synchrotron x-ray powder diffraction pattern collected at various pressure (indicated) up to 14 GPa. (b) The enlarged view around the most intense Bragg peak region. The miller indices of both major peaks are given in the bottom-most in (b). The “P (GPa)” represents the pressure in the GPa unit. The topmost pattern labeled by “0.50 (release)” was collected during releasing the pressure with effective pressure of 0.50 GPa. 181

Figure 6.17: Pressure-dependence of (a) in-plane and (b) out of plane lattice parameters of NiMnGa. The red line and dotted blue line in (a) and (b) represent the linear compression and extrapolated region of linear compression behavior, respectively. The “ da/dP ” and “ dc/dP ” indicate the linear compression rate in a and c -parameter in (a) and (b), respectively. The error in lattice parameters is smaller than the symbol size. (c) The unit cell of NiMnGa, wherein different lengths of springs connected with arrows indicate the different compression rates in the in-plane and out-of-plane lattice parameters..... 183

Figure 6.18: Pressure-dependence of unit cell volume (V). Solid lines indicate the results of a second-order Birch–Murnagan equation-of-state (EoS) fit to the data. “EoS1” and “EoS2”

represent the fitting considering the data upto 4 GPa and above 4 GPa, respectively. The V_0 , B , and B' are the parameters obtained from the fit. Pressure dependence of c/a ratio is depicted in the inset, wherein the red line and dotted blue line represent the linear fit and extrapolation of the linear fit, respectively. The error in V and c/a are smaller than the symbol size. 184

Figure 7.1: Temperature dependence of the real part of ac-susceptibility ($\chi'(T)$) of NiMnGa, measured at 333 Hz under the zero-field cooled warming cycle. The T_C and T_{SRT} indicate the ferromagnetic and spin reorientation transition temperature, respectively..... 194

Figure 7.2: (a) The variation of the real component of ac-susceptibility (χ') with dc magnetic field (H) (χ' vs H plot) at 220 K with increasing and decreasing field (-1 T to 1 T). H_S and H_C indicate the critical fields at which the system transforms from helical to biskyrmions and from biskyrmions to ferromagnetic states, respectively. (b) The first derivative ($d\chi'/dH$) of χ' vs H plot. The insets (i) & (ii) of (b) depict an enlarged view around -0.25 T and 0.25 T, respectively, where the vertical dashed lines indicate the increasing and decreasing fields of maxima and minima. 196

Figure 7.3: The variation of the real component of ac-susceptibility (χ') with dc magnetic field (H) (χ' vs H plot) at the indicated temperatures (5 to 340 K) with increasing magnetic field only (0 to ± 1 T). The inset shows the enlarged view around 0.2 T. The blue arrow in the inset indicates the increasing behavior of critical field (H_S) and peak growth on decreasing the temperature..... 198

Figure 7.4: The observed profile (black spheres), calculated profile (continuous red line), difference profile (continuous green line), Bragg peak positions (blue ticks), and weighted agreement factor (R_w) obtained after Rietveld refinement in the $P6_3/mmc$ space group of NiMnGa using high-Q synchrotron x-ray powder diffraction data at (a) 400 K, (b) 300 K, and (c) 100 K. The reduced structure function $F(Q)$ vs Q at (d) 400 K, (e) 300 K, and (f) 100 K. 200

Figure 7.5: Experimental pair distribution functions (PDFs; $G(r)$) on the vertically spaced scale at various temperatures from 400 K to 100 K in the (a) Short-range (SR), (b) Medium-range (MR), and (c) Long-range (LR) regimes. 202

Figure 7.6: The experimental PDF (blue spheres), calculated PDF (continuous red line), their difference (continuous green line at the bottom), and weighted agreement factor (R_w) obtained by real-space structure refinements using the $P6_3/mmc$ space group in the SR and LR at (a) 400 K, (b) 300 K and (c) 100 K with isotropic atomic displacement parameters (ADPs; U_{iso}) consideration in the refinements. The PDFs fits in the SR and LR using the same space group ($P6_3/mmc$) at (d) 400 K, (e) 300 K, and (f) 100 K with anisotropic ADPs (U_{aniso}) consideration in the refinements.

The significant misfit just below 5 Å is indicated by encircled region of difference PDFs (Gdiff) in (d), (e), and (f)..... 206

Figure 7.7: The anisotropic atomic displacement parameter (AADP) of the Mn atom with distance (r) obtained after r -dependent real-space structure refinement using the $P6_3/mmc$ space group at (a) 400 K, (b) 300 K, and (c) 100 K. The planer ADP (U_{11}) and prismatic ADP (U_{33}) are indicated by black squares connected with a solid line and blue spheres connected with a solid line, respectively. The insets in the (a), (b), and (c) depict the ratio of U_{33} with U_{11} (i.e., U_{33}/U_{11}) vs r plot. 207

Figure 7.8: The experimental PDF (blue spheres), calculated PDF (continuous red line), their difference (continuous green line at the bottom), and weighted agreement factor (R_w) obtained by real-space structure refinements in the SR at 300 K using space group (a) $P6_3mmc$, (b) $P\bar{6}m2$, (c) $P6_3mc$, (d) $P\bar{6}2c$, (e) $P6_322$, (f) $P6_3/m$, (g) $P\bar{3}1c$, (h) $Pmmc$, (i) $Pnma$, (j) $P\bar{3}m1$, and (k) $P3m1$. For comparison, the difference PDF (Gdiff) of (j) and (k) are depicted in separate panels given below (j) and (k), respectively. 209

Figure 7.9: The experimental PDF (blue spheres), calculated PDF (continuous red line), their difference (continuous green line at the bottom), and weighted agreement factor (R_w) obtained by real-space structure refinements using the $P6_3/mmc$ space group in the SR at (a) 400 K and (c) 100 K, while in the LR at (e) 400 K and (g) 100 K. The PDFs fits using the $P3m1$ space group in the SR at (b) 400 K and (d) 100 K, while in the LR at (f) 400 K and (h) 100 K..... 214

List of Tables

Table 3.1: Interatomic distances corresponding to the refined structural parameters of the austenite phase at 300 K and premartensite phase at 230 K reported in the literature[71].	82
Table 3.2: Parameters obtained from the PDF refinement using cubic austenite ($Fm\bar{3}m$) and $3M$ commensurate premartensite ($Pnmm$) structures in the SR regime at selected temperatures. The a , b , c are the lattice parameters, U_{iso} is the isotropic atomic displacements parameter, δ_2 is the coefficient for $1/r^2$ contribution to the peak sharpening, and R_w is the weighted agreement factor for the PDF refinement.	87
Table 6.1: The lattice parameters (a and c), thermal factor (B), and agreement factors obtained after Rietveld refinement (with $P6_3/mmc$ space group) using temperature dependent SXRPD data of NiMnGa.	166
Table 6.2: Comparison of lattice parameters (a and c) with temperature and pressure of hexagonal NiMnGa.	186
Table 7.1: The lattice parameters (a and c), thermal factor (B), and agreement factors obtained after Rietveld refinement (with $P6_3/mmc$ space group) using temperature dependent high- Q SXRPD data of NiMnGa.	201
Table 7.2: The lattice parameters (a and c), isotropic atomic displacements parameters (U_{iso}), the coefficient for $1/r^2$ contribution to the peak sharpening (δ_2), and weighted agreement factor (R_w) obtained from the PDF refinement using hexagonal ($P6_3/mmc$ space group) at the selected temperatures of NiMnGa.	204
Table 7.3: The lattice parameters (a and c), anisotropic atomic displacements parameters ($U_{11} = U_{22}$ and U_{33}), the coefficient for $1/r^2$ contribution to the peak sharpening (δ_2), and weighted agreement factor (R_w) obtained from the PDF refinement using hexagonal ($P6_3/mmc$ space group) at the selected temperatures of NiMnGa.	205
Table 7.4: List of subgroups of $P6_3/mmc$ (194), their asymmetric unit, Wyckoff positions[415], and weighted agreement factor (R_w) of the real-space structure refinement of NiMnGa. The $P6_3/mmc$ (194) is not the subgroup. It is added just given for the comparison of Wyckoff positions and R_w .	210
Table 7.5: The lattice parameters (a and c), isotropic atomic displacements parameters (U_{iso}), coefficient for $1/r^2$ contribution to the peak sharpening (δ_2), atomic positions and weighted	

agreement factor (R_w) obtained from the PDF refinement in the SR using trigonal structure with $P3m1$ space group at the selected temperatures of NiMnGa. 212

List of Abbreviations

Anisotropic Atomic Displace Parameters	AADP
Alternating Current	ac
Atomic Displace Parameters	ADP
Antiferromagnetic	AFM
Anomalous Hall Conductivity	AHC
Anomalous Hall Effect	AHE
Anomalous Thermal Expansion	ATE
Austenite and Premartensite	A+PM
Body Centered Cubic	BCT
Birch–Murnagan Equation-of-State	B-M EoS
Backscattered Electrons	BSE
Cryogenic Free Measurement System	CFMS
Diamond Anvil Cell	DAC
Direct Current	dc
Dzyaloshinskii-Moriya Interactions	DMI
Density of States	DOS
Differential Scanning Calorimetry	DSC
Energy Dispersive Analysis of X-rays	EDAX
Energy Dispersive Spectroscopy	EDS
Electrical Transport Option	ETO
Field Cooling	FC

Face Centered Cubic	FCC
Field Cooled Warming	FCW
Ferromagnetic	FM
Formula Unit	f. u.
Full-Width at Half-Maxima	FWHM
Hour	h
High-Resolution Transmission Electron Microscope	HRTEM
Inelastic Neutron Scattering	INS
Lattice Parameters	LP
Long-Range	LR
Long-Range Ordered	LRO
Lorentz Transmission Electron Microscopy	L-TEM
Magnetocrystalline Anisotropy	MCA
Magnetic Field Induced Strain	MFIS
Minute	min
Magnetoresistance	MR
Magnetic Properties Measurement System	MPMS
Magnetic Shape Memory Alloy	MSMA
Magnetic Shape Memory Effect	MSME
Martensite Phase Transition	MPT
Ordinary Hall Effect	OHE
Pair Distribution Function	PDF
Premartensite	PM

Premartensite Phase Transition	PMT
Physical Properties Measurement System	PPMS
Positive Thermal Expansion	PTR
Sample to Detector Distance	SDD
Secondary Electrons	SE
Scanning Electron Microscope	SEM
Shape Memory Alloy	SMA
Shape Memory Effect	SME
Superconducting Quantum Interference Device	SQUID
Short-Range	SR
Short-Range Ordered	SRO
Spin Reorientation Transition	SRT
Synchrotron X-ray Powder Diffraction	SXRPD
Thermal Expansion Coefficient	TEC
Topological Hall Effect	THE
Vibrating Sample Magnetometer	VSM
X-ray Diffraction	XRD
Zero-Field Cooled Warming	ZFCW
Zero Thermal Expansion	ZTE
Two Dimensional	2D
Second-Order	2 nd O

List of Symbols

Area	A
Austenite Finish Temperature	A_f
Austenite Start Temperature	A_s
Thermal Factor	B
Bulk Modulus	B
Pressure Derivative of Bulk Modulus	B'
Fermi Energy	E_F
Reduced Structure Function	$F(Q)$
Gibbs Free Energy	G
Pair Distribution Function	$G(r)$
Calculated Pair Distribution Function	G_{cal}
Difference Pair Distribution Function	G_{diff}
Experimental Pair Distribution Function	G_{exp}
Magnetic Field	H
Current	I
Intensity	$I(Q)$
Measured Intensity	$I_m(Q)$
Boltzmann Constant	k_B
Incident Wave Vector	k_i
Reflected Wave Vector	k_f
Magnetic Anisotropy Constant	K_u

Length	L
Magnetization	M
Spontaneous Magnetization	M_S
Martensite Start Temperature	M_s
Martensite Finish Temperature	M_f
Magnetic Field Dependent Magnetization	$M(H)$
Temperature Dependent Magnetization	$M(T)$
Pressure	P
Magnitude of Scattering Vector	Q
Maximum Value of Scattering Vector	Q_{max}
Maximum Instrumental Q -value	$Q_{maxinst}$
Minimum Value of Scattering Vector	Q_{min}
Distance	r
Resistance	R
Ordinary Hall Coefficient	R_0
Anomalous Hall Coefficient	R_S
Scaling Coefficient	S_H
Total Scattering Structure Function	$S(Q)$
Time	t
Temperature	T
Curie Temperature	T_C
Curie Temperature of the Martensite Phase	T_C^M
Martensite Transition Temperature	T_M

Onset of Curie Temperature	T_{onset}
Premartensite Transition Temperature	T_{PM}
Spin Reorientation Transition Temperature	T_{SRT}
Isotropic Atomic Displacement Parameter	U_{iso}
Unit Cell Volume	V
Valence Electron Concentration Per Atom	e/a
Isothermal Entropy Change	ΔS_{iso}
Peak Value of Isothermal Entropy Change	ΔS_{pk}
Change in Temperature	ΔT
Change in Volume	ΔV
Wavelength	λ
Angstrom	Å
Grüneisen Parameter	γ
Magnetic Flux	ϕ
Phase Shift	Φ
Resistivity	ρ
Magnetic Permeability of Free Space	μ_0
Anomalous Hall Resistivity at Zero-field	ρ_{AH}
Anomalous Hall Resistivity	ρ_{AHE}
Longitudinal Resistivity	ρ_{xx}
Hall Resistivity	ρ_{xy}
Calculated Hall Resistivity	ρ_{xy}^{cal}

Experimental Hall Resistivity	ρ_{xy}^{exp}
Topological Hall Resistivity	ρ_{xy}^T
Maxima of Topological Hall Resistivity	ρ_{xy}^{Tmax}
Anomalous Hall Conductivity	σ_{AH}
Intrinsic Anomalous Hall Conductivity	σ_{AH}^{in}
Longitudinal Conductivity	σ_{xx}
Hall Conductivity	σ_{xy}
Twinning Stress	σ_{tw}
External Stress	σ_{ext}
AC-susceptibility	χ
Real Part of AC-susceptibility	χ'
Temperature Dependent AC-susceptibility	$\chi(T)$
Magnetic Field Dependent AC-susceptibility	$\chi(H)$
Correlation length	ξ
Debye Temperature	Θ_D
Bohr Magnetron	μ_B
Maximal Strain	ϵ_0
Correlation Parameter	δ_2
Rescaled Temperature	θ
Bragg Angle	2θ
Spin-Orbit Interaction Energy	ϵ_{SO}

Preface

Shape memory alloys (SMAs) are a special class of materials that remember their shape with the application of temperature and (or) stress. The shape change in these materials, which can be manipulated by both temperature and stress, is directly related to a structural (martensite) phase transition. These alloys have received tremendous interest due to their extensive technological applications ranging from automobiles, aerospace, marine structures, biomedical devices to energy conversion devices. Recently, another kind of SMAs gained huge interest, where shape change can be manipulated, and a large strain can be generated with the application of external magnetic field. These materials are termed magnetic shape memory alloys (MSMAs). The MSMAs have the advantage over the conventional SMAs as large strain can be generated within the martensite phase with magnetic field, which provides faster switching. Thus, the discovery of MSMAs offers potential for developing novel sensors and actuators based on the application/removal of the magnetic field with or without external stress at a fixed temperature. Among the several MSMAs, the Ni-Mn-based MSMAs are of current interest as, besides a large magnetic field induced strain (MFIS), they also exhibit several exotic physical properties/phenomena, e.g., giant magnetocaloric effect, large magnetoresistance, anomalous Nernst effect, strain glass transition, skyrmionic textures etc. These exotic properties/phenomena of Ni-Mn-based MSMAs make these materials very important for solid-state cooling and information storage technology applications also.

The origin of the above-mentioned properties of Ni-Mn-based MSMAs is closely related to their interesting phase transition behavior. These alloys exhibit a paramagnetic to ferromagnetic (FM) phase transition and sometimes include FM to antiferromagnetic and (or) ferrimagnetic phase transition. Besides the magnetic phase transitions, they also show a structural phase transition from the high temperature cubic austenite to a low-temperature lower-symmetry martensite phase. In

general, the martensite phase of Ni-Mn-based MSMA exhibits structural modulation, which plays a vital role in the appearance of huge strains in these alloys. Therefore, it is important to understand the phase transitions and crystal structure of different phases in order to explore the different physical properties of Ni-Mn-based MSMA.

Some important Ni-Mn-based MSMA (e.g., Ni_2MnGa) show an interesting precursor (or premartensite) phase, which precedes the martensite phase, with preserved cubic symmetry of the austenite phase. As premartensite phase is directly related to the martensite phase, it also affects the related physical properties (e.g., strain glass behavior and skyrmionics textures) observed in these alloys. Therefore, a detailed understanding of the premartensite phase is necessary to tune the related physical properties of the martensite phase. Although the precursor have been observed in the austenite phase also in terms of the appearance of diffuse scattering and softening of $1/3$ (110) transverse acoustic (TA_2) phonon mode in Ni_2MnGa due to the development of local short-range correlations, it is still unclear whether these precursor effects are related to the martensite or the premartensite phase. This calls for a systematic study of the local structure of these alloys. In addition, since the premartensite phase usually appears in a rather narrow temperature range with weak signatures in the bulk physical property measurements, a premartensite phase stable over a wider temperature window is desirable for a proper understanding of this state. The results presented in this thesis provide evidence for a precursor state of the premartensite phase as local structure in the austenite phase of Ni_2MnGa MSMA, where the stability of the premartensite phase is narrow and robust evidence for the stabilization of the premartensite phase as ground state of the Ni-Mn-In MSMA via chemical pressure tuning using magnetization and high-resolution, high-flux as well as high- Q synchrotron x-ray diffraction data analysis.

In recent years, additional contributions (anomalous and topological) to the conventional Hall effect have been reported in Ni-Mn-based MSMA. The results presented in the literature for the Hall effect are, however, controversial and calls for a detailed investigation of these MSMA. The existing literature also suggests that the topological Hall effect associated with skyrmions may be influenced by the premartensite phase. Therefore, it is essential to investigate the role of the premartensite phase on the topological Hall effect in these alloys. In the present thesis, results of a comprehensive study on the origin of the anomalous and topological Hall effect in Ni₂MnGa MSMA is presented using analysis of magnetotransport data.

The hexagonal compound NiMnGa, which comes under another class of related materials, has received vast attention due to the observation of stable biskyrmionic textures, which can be utilized in the skyrmion-based spintronic devices at higher temperatures. Although temperature dependent structural and magnetic studies have been performed in the past, a detailed investigation of the correlation between the structural and magnetic behavior is still unclear in this compound. Interestingly, the stability of skyrmionic textures in some of the materials is found to be very sensitive to external uniaxial stress or pressure. This suggests that the stability of the skyrmionic spin textures can be manipulated through spin-lattice/magnetoelastic coupling. The manipulation of skyrmions with external pressure provides an additional tool for manipulating the functionality of such compounds. Thus, a detailed study of the hexagonal compound NiMnGa with external hydrostatic pressure may provide important information, which can be useful for the applications in spintronic devices. The present thesis provides results of a comprehensive study of phase transitions on NiMnGa using magnetization as well as temperature and pressure dependent synchrotron x-ray diffraction data. In general, the stabilization of skyrmions have been proposed to exist in noncentrosymmetric materials due to the presence of Dzyaloshinskii–Moriya interaction.

However, the NiMnGa has a hexagonal structure with a centrosymmetric space group ($P6_3mmc$) and yet it hosts biskyrmionic textures. To understand the origin of biskyrmions in this compound, the results of a local structure study of the NiMnGa using high- Q synchrotron x-ray diffraction data analysis are also presented in this thesis.

In this thesis, a detailed study of the phase transition, local as well as global crystal structure, and anomalous Hall effect are performed in Ni₂MnGa, Ni₅₀Mn₃₄In_{16-x}Al_x ($x = 0.5, 0.8$) MSMA, and a related hexagonal NiMnGa system. The present thesis is divided into eight chapters.

Chapter 1 provides definition and a detailed description of martensite transition, shape memory alloys, magnetic shape memory alloys and related terms used in this work, followed by a review of literature related to the Ni-Mn-based MSMA and hexagonal NiMnGa.

Chapter 2 contains the details of the synthesis process, including a detailed discussion of various components, several characterization techniques employed, e.g., laboratory source x-ray diffraction measurements for checking the phase purity, energy dispersive analysis of x-rays for composition determination, differential scanning calorimetry for the phase transition temperatures.

In addition, the details of the magnetic and magnetotransport measurements using physical properties, magnetic properties, and cryogenic free measurement systems are provided. The details of the synchrotron x-ray powder diffraction (SXRPD) measurements carried out at the P02.1 beamline of PETRA-III and Xpress beamline of ELETTRA at different temperatures and pressures, respectively, are also presented in this chapter.

Chapter 3 provides evidence for the precursor state of the premartensite phase in Ni₂MnGa MSMA using atomic pair distribution function analysis of the high- Q SXRPD data and magnetization studies. This precursor state is present in the short-range only with a crystal structure similar to the premartensite phase. The Arrott plot, critical isotherms and universal curve analysis

confirm the first-order character of paramagnetic to FM phase transition in Ni₂MnGa MSMA, while the analysis of the high-resolution SXRPD data reveals the presence of magnetoelastic coupling. The role of such a coupling in inducing first-order FM phase transition is rationalized using the Landau theory considerations.

Chapter 4 presents evidence for intrinsic anomalous Hall conductivity as well topological Hall effect in Ni₂MnGa MSMA. A detailed analysis of Hall conductivity reveals that intrinsic Berry curvature contribution dominates over skew scattering and side jump in the austenite, premartensite and martensite phases of Ni₂MnGa MSMA. The presence of skyrmions is indicated in the martensite as well as the premartensite phases by the observation of characteristic temperature-independent behavior of the peak value of the topological Hall resistivity.

Chapter 5 describes the results of a detailed structural and magnetic investigation of the effect of Al-substitution in Ni₅₀Mn₃₄In₁₆ MSMA using SXRPD and magnetization data. The combined analysis of magnetization and SXRPD data reveal that the premartensite phase is stabilized over a wide temperature range in Ni₅₀Mn₃₄In_{15.2}Al_{0.8} MSMA. This robust evidence for the stabilization of the premartensite phase is shown to result by tuning of the chemical pressure via substitution with a smaller size atom (Al) at the In site in Ni₅₀Mn₃₄In₁₆ MSMA. The structure of stabilized premartensite phase is shown to be $3M$ modulated monoclinic in the $P2/m$ space group. The analysis of the SXRPD data measured under the magnetic field provides evidence for the presence of magnetoelastic coupling, which plays a crucial role in the stabilization of the PM phase in Ni₅₀Mn₃₄In₁₆ MSMA by Al substitution.

Chapter 6 presents the results of magnetization data and a detailed crystal structure investigation using SXRPD on the biskyrmion host hexagonal NiMnGa compound. The Arrott plots analysis and presence of small thermal hysteresis around FM T_C in the magnetization data reveal first-order

character of the paramagnetic to FM phase transition in this compound. We also presented evidence for magnetoelastic coupling at the FM as well as the spin reorientation transitions (SRT). It is argued that the Ni-Mn and Ni-Ga mediated exchange interactions dominate the paramagnetic to the FM phase transition, while the Mn-Mn mediated exchange interactions dominate the SRT. In addition, the evidence for an isostructural phase transition driven by hydrostatic pressure at a pressure around 4 GPa in the hexagonal NiMnGa using pressure dependent SXRPD data analysis is also presented in this chapter.

Chapter 7 provides the signature of biskyrmionic states in NiMnGa using magnetic field-dependent ac-susceptibility measurements and a detailed analysis of the local structure of NiMnGa using the pair distribution function method. A high- Q SXRPD data reveals the presence of noncentrosymmetric trigonal structure with space group $P3m1$ in the short-range, which may be responsible for the presence of the biskyrmionic state. On the other hand, the long-range structure of NiMnGa remains centrosymmetric hexagonal with $P6_3/mmc$ space group.

Chapter 8 summarizes the key findings of the present thesis and proposes a few suggestions for future work in the field related to this study.